

# Acousto-electric transport in epitaxial monolayer graphene on SiC

P. V. Santos,<sup>a)</sup> T. Schumann, M. H. Oliveira, Jr., J. M. J. Lopes, and H. Riechert  
 Paul-Drude-Institut für Festkörperelektronik, Hausvogteiplatz 5-7, 10117 Berlin, Germany

(Received 8 March 2013; accepted 21 May 2013; published online 5 June 2013)

We report on the piezoelectric excitation and acoustic charge transport by gigahertz surface acoustic waves (SAWs) in epitaxial monolayer graphene (EG) on SiC. The GHz SAWs frequencies were generated by interdigital transducers fabricated on a piezoelectric island on the SiC substrate. Acoustic transport studies in a Hall bar geometry show that the propagating SAW field transports carriers in EG, the transport direction being determined by the direction of the acoustic beam. Carrier transport is driven by drift in the piezoelectric field induced by the SAW in EG. © 2013 AIP Publishing LLC.  
[\[http://dx.doi.org/10.1063/1.4809726\]](http://dx.doi.org/10.1063/1.4809726)

Graphene is emerging as an important material for electronic applications due to its two dimensional, planar character and the high carrier mobility, which persists up to room temperatures.<sup>1</sup> These favorable properties open the way for exploring carrier control processes alternative to the direct application of electric fields. A particularly interesting approach employs the strain and piezoelectric fields generated by a surface acoustic wave (SAW). A SAW propagating on a graphene layer generates a moving strain field with  $\mu\text{m}$  dimensions and tunable amplitude, which can control the carrier mobility by modulating the graphene band structure.<sup>2</sup> In piezoelectric materials, the SAW strain is accompanied by a piezoelectric potential, which can capture carriers and transport them with the acoustic velocity. Contrary to the conventional drift and diffusion process under an electric field, the moving potentials maintain the shape of the carrier packages and enable the control of the carrier density down to the single carrier level.<sup>3</sup>

Applications combining graphene and SAWs include sensors based on the change of acoustic properties by light absorption<sup>4</sup> or upon the adsorption of gaseous species on a graphene layer transferred to a piezoelectric substrate.<sup>5</sup> The moving piezoelectric field induced by a SAW has been shown to induce carrier transport in carbon nanotubes.<sup>6,7</sup> The effects of SAW fields on the graphene band structure has been theoretically addressed by Thalmeier *et al.*<sup>8</sup> Recently, Misekis *et al.*<sup>9</sup> have demonstrated SAW-induced carrier transport in graphene. These studies were carried out on graphene layers transferred to a piezoelectric substrate sustaining SAWs with a frequency of a few hundreds of MHz.

In this work, we report on the generation of GHz SAWs as well as on the acoustically induced transport of carriers in epitaxial monolayer graphene (EG) on SiC substrates. The formation of large area graphene sheets by silicon sublimation<sup>10,11</sup> from the SiC surface enables the production of high quality layers directly on an insulating SiC wafer, which can be processed to devices using conventional planar fabrication techniques. The SAWs were generated by interdigital transducers (IDTs) fabricated on piezoelectric ZnO islands selectively deposited on EG. By taking advantage of the high acoustic velocity of SiC, we demonstrate the generation of SAWs with frequencies above 2.4 GHz using a conventional

photolithographic process. These SAW frequencies are substantially higher than those previously reported for acoustic waves on graphene.<sup>9</sup> Acoustic transport studies in a Hall bar geometry show that the SAWs transport carriers in EG, with the transport direction being determined by the direction of the acoustic beam. The driving mechanism for transport has been identified as the drift in the moving piezoelectric field induced by the SAW strain field in the semi-insulating SiC substrate.

The EG samples were prepared on  $10 \times 10 \text{ mm}^2$  semi-insulating 4H-SiC (0001) substrates by Si sublimation in a 900 mbar Ar atmosphere at a temperature of  $1600^\circ\text{C}$  for 15 min. Details of the graphene formation process can be found in Ref. 12. The SAWs were generated by IDTs (cf., Fig. 1(a)) photo-lithographically patterned on the sample surface. Due to the small piezoelectricity of the SiC substrates, the IDTs were fabricated on islands consisting of a 350 nm-thick piezoelectric ZnO on a 50 nm  $\text{SiO}_2$  buffer sputtered on the sample surface. In order to avoid degradation of the EG layer, the ZnO/ $\text{SiO}_2$  layer stack was selectively sputtered through a shadow mask. As an additional benefit, the shadow mask produces a smooth thickness gradient at the edges of the sputtered islands, which improves the SAW transmission to the SiC area outside the island. Acoustic delay lines consisting of two aluminum single-finger IDTs for an acoustic wavelength  $\lambda_{\text{SAW}} = 2.8 \mu\text{m}$  were then deposited on the piezoelectric island using contact lithography. Due to the hexagonal symmetry of the EG/SiC-4H structures, the SAW properties do not depend on the orientation of the delay lines on the sample surface. The  $160 \mu\text{m}$  long IDTs have an aperture of  $84 \mu\text{m}$  and are separated by 6 mm. For the electrical measurements, the EG layer was structured in the form of a  $10 \mu\text{m}$ -wide Hall bar with metal contact pads.

Raman spectra recorded after sample processing show intense G and 2D-lines (cf., Fig. 1(b)) thus indicating that the graphene layer in the Hall bar is essentially not affected by the processing steps. The Raman signal in the  $1250\text{--}1500 \text{ cm}^{-1}$  is assigned to the underlying buffer layer.<sup>13</sup> The electric properties of the processed sample were probed by low-temperature magnetotransport measurements revealing an electron density  $n_{2D} = 2 \times 10^{12} \text{ cm}^{-2}$  and a mobility  $\mu = 1000 \text{ cm}^2/(\text{Vs})$  at 330 mK.

The excitation of SAWs is demonstrated by measurements of the radio-frequency (rf) power reflection coefficient

<sup>a)</sup>E-mail: santos@pdi-berlin.de

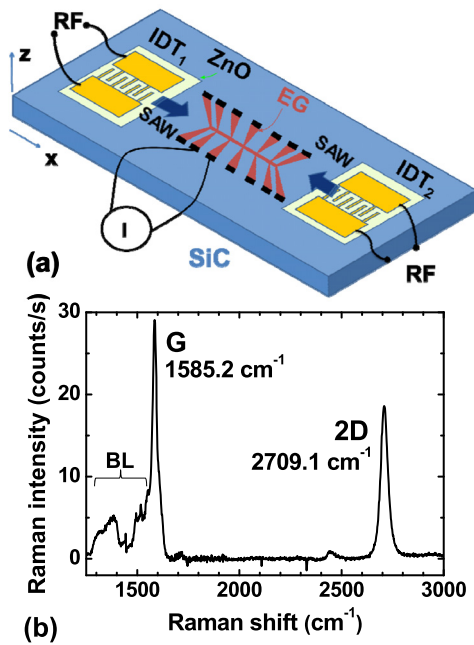


FIG. 1. (a) Experimental setup for SAW generation on EG on 4H-SiC. The SAWs are generated by applying an rf-power to IDTs deposited on a piezoelectric ZnO island. The graphene layer is structured in the form of a Hall bar for acousto-electric measurements. (b) Raman spectrum measured on the Hall bar after sample processing showing the characteristic *G* and *2D* peaks. The features between 1200 and 1650  $\text{cm}^{-1}$  (BL) are attributed to the carbon buffer layer underneath EG. The full widths at half maximum of the *G* and *2D* lines are 24 and 37  $\text{cm}^{-1}$ , respectively. The SiC-background has been subtracted.

$s_{11}$  for the SAW delay lines illustrated in Fig. 2(a).  $s_{11}$  corresponds to the ratio between the reflected and forward rf-power applied to the IDT. The dips in its spectral dependence signalize the conversion of electrical into acoustic power during the generation of the two Rayleigh modes with frequencies of 1.87 GHz (mode  $M_1$ ) and 2.40 GHz (mode  $M_2$ ). Mode  $M_1$  is the lowest energy SAW mode with acoustic energy strongly confined within the ZnO/SiO<sub>2</sub> stack, which has an effective acoustic velocity much lower than the one of the SiC substrate.  $M_2$  is an overtone with a longer field penetration into the substrate. The inset of Fig. 2(a) compares the measured velocity of the modes in the ZnO/SiO<sub>2</sub>/SiC structure (symbols, obtained from the ratio between  $\lambda_{\text{SAW}}$  and the IDT resonance frequency) with the ones calculated using a continuum elastic model for the multilayer (lines).<sup>14,15,20,21</sup> The calculations, which were carried out using the nominal thicknesses of the sputtered layers, slightly underestimate the SAW velocities. This discrepancy is probably due to an overestimation of the thicknesses of the layers sputtered through the shadow mask.

Experimental evidence for SAW propagation between the two IDTs was obtained by measuring the time-dependence of the rf power reflection ( $s_{11}$ ) and transmission ( $s_{21}$ ) coefficients of the delay lines using a network analyzer with Fourier transform capability (cf., Fig. 2(b)). The  $s_{11}$  time profile shows an echo at twice the SAW transit time ( $t_t$ ) between the IDTs due to SAW reflection at the opposite IDT. The peaks in rf power transmission coefficient  $s_{12}$  (for  $M_1$ ) at the delays  $t_t$  and  $3t_t$  correspond to one and three (triple transient) transit times, respectively. The weaker structure at

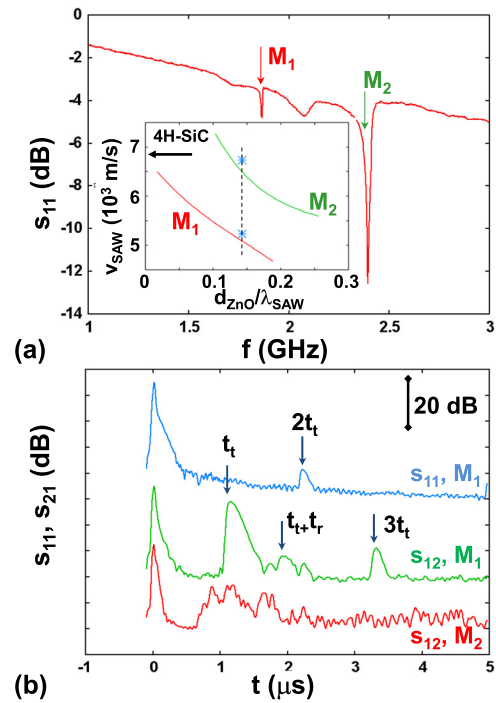


FIG. 2. (a)  $s_{11}$  radio-frequency (rf) power reflection coefficient for a delay line on an EG-coated 4H-SiC substrate. The inset displays the dependence of the calculated (lines) and measured (symbols) velocities for modes  $M_1$  and  $M_2$  as a function of the ZnO thickness (the horizontal arrow indicates the SAW velocity in 4H-SiC). (b) Time delay profiles during acoustic propagation. The arrows mark the echo times for one ( $t_t$ ), two ( $2t_t$ ), and three ( $3t_t$ ) SAW transits between the two IDTs as well as for waves which are detected after a reflection at the sample borders ( $t_t + t_r$ ). The curves are shifted vertically for clarity.

a delay  $t_t + t_r$  has been associated to a SAW, which is emitted by IDT<sub>1</sub> in the  $-x$  direction (cf., Fig. 1(a)) and then reflected at the sample border before being detected by IDT<sub>2</sub>.

The acousto electric transport measurements were carried out by detecting the current  $I$  flowing between two Hall-bar contacts, as indicated in Fig. 1(a). The experiments were performed at room temperature by chopping the rf-power applied to one IDT at a frequency of 400 Hz and synchronously measuring the current using a lock-in amplifier. The left and right panels in Fig. 3 displays the frequency dependence of the acousto-electric current induced by modes  $M_1$  and  $M_2$ , respectively, measured for different nominal powers  $P_{\text{rf}}$  applied to IDT<sub>1</sub>. We confirmed that the conduction takes place through the EG layer (rather than through the underlying substrate) by carrying out control measurements on a sample, where the graphene layer was removed prior to the metalization process (curve “no EG” for  $P_{\text{rf}} = 17$  dBm in Fig. 3). The current completely vanished in this case.

The current induced by mode  $M_1$  increases monotonically with  $P_{\text{rf}}$  and becomes proportional to  $P_{\text{rf}}$  in the region of high acoustic powers (Fig. 4). The current flow also depends on the SAW propagation direction, as illustrated in the curves of Fig. 4(b), which were recorded by exciting either IDT<sub>1</sub> or IDT<sub>2</sub> of the delay line of Fig. 1(a). The different current amplitudes in the two cases are attributed to differences in the transduction efficiencies of the two IDTs. Mode  $M_2$  has a more complicated power dependence. The current in this case initially increases, reaches a maximum, and then

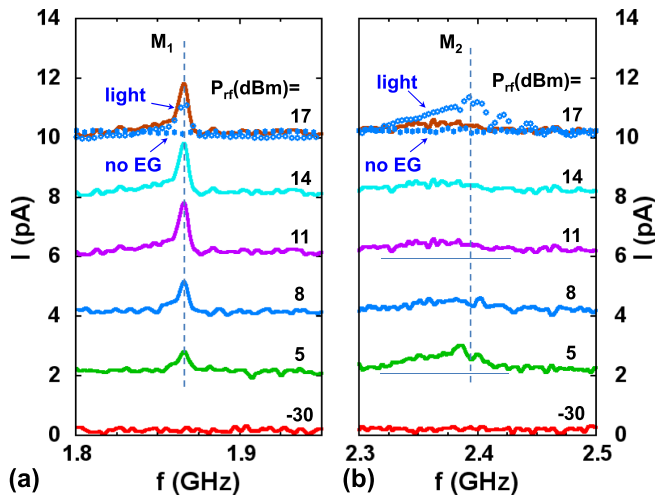


FIG. 3. Spectral dependence of the current ( $I$ ) measured between two Hall bar contacts (cf., Fig. 1(a)) as a function of the nominal rf-power ( $P_{rf}$ ) applied to the IDT for the modes (a)  $M_1$  and (b)  $M_2$  indicated in Fig. 2(a). The symbols denoted by “light” display the current measured under illumination. The symbols denoted by “light” (open circles) and “no EG” (dots) display the current measured under illumination and on a control sample where the EG was removed during processing, respectively. The curves are displayed vertically for clarity.

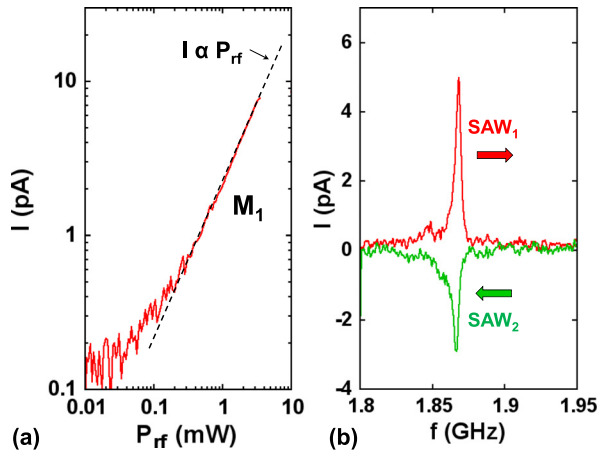


FIG. 4. Dependence of the current ( $I$ ) acoustically induced by mode  $M_1$  on (a) SAW power and (b) propagation direction.

reduces for larger  $P_{rf}$ . In addition, the current induced by this mode is much more sensitive to illumination than in case of mode  $M_1$ . This behavior is illustrated by the curve marked *light*, which was recorded by illuminating the sample using a weak visible light source. The enhanced current is probably due to the creation of free carriers in the graphene layer via the excitation of defect centers in the underlying SiC substrate.

Since SiC is a weakly piezoelectric material, one interesting question is the relative contribution for transport from the moving modulations by the SAW strain and piezoelectric fields. The strain induced in the plane of EG by a Rayleigh SAW has a single component with amplitude  $u_{xx}^{(s)}$  ( $\mathbf{u} \equiv$  elastic displacement field), which induces a periodic energy modulation of the electronic levels along the SAW propagation direction ( $x$ ) given by  $\Delta E_{DP} = g u_{xx}^{(s)}$ . Here,  $g$  is the deformation potential (DP),<sup>16</sup> and we have neglected

the small contribution to  $\Delta E_{DP}$  from the gauge field mechanism.<sup>16,17</sup> If  $\Phi_{SAW}^{(s)}$  denotes the amplitude of the piezoelectric potential induced on the EG graphene plane, then the ratio  $r_m$  between the two modulation amplitudes becomes<sup>18</sup>  $r_m = \Delta E_{DP} / (e \Phi_{SAW}^{(s)})$ , where  $e$  is the electron charge. Using the ratio  $u_{xx}^{(s)} / \Phi_{SAW}^{(s)}$  calculated using the previously mentioned continuum model and assuming values for  $g$  in the range from 4 to 30 eV,<sup>16,19</sup> we obtain  $r_m \approx 0.1 - 0.5 < 1$ . Despite the small piezoelectricity, the main driving force for carrier motion is, therefore, provided by the SiC piezoelectricity. The linear dependence of the current on  $P_{rf}$  in Fig. 4(a) arises from the fact that both the transport field and the piezoelectrically charge induced in EG are proportional to  $\sqrt{P_{rf}}$ .

In conclusion, we have introduced a process for the generation of GHz surface acoustic fields in epitaxial graphene on SiC. The structures were used to investigate the acoustic charge transport in graphene, which has been shown to be driven by the piezoelectricity of the SiC substrate.

We thank F. Grosse for discussions and comments as well as S. Rauwerdink, W. Seidel, and A. Tahraoui for the assistance in the preparation of the samples.

<sup>1</sup>A. K. Geim and K. S. Novoselov, *Nat. Mater.* **6**, 183 (2007).

<sup>2</sup>C.-H. Park, Y.-W. Son, L. Yang, M. L. Cohen, and S. G. Louie, *Nano Lett.* **8**, 2920 (2008).

<sup>3</sup>J. M. Shilton, V. I. Talyanskii, M. Pepper, D. A. Ritchie, J. E. F. Frost, C. J. B. Ford, C. G. Smith, and G. A. C. Jones, *J. Phys.: Condens. Matter* **8**, L531 (1996).

<sup>4</sup>V. S. Chivukula, D. Ciplys, J. H. Kim, R. Rimeika, J. M. Xu, and M. S. Shur, *IEEE Trans. Ultrason. Ferroelect. Freq. Control.* **59**, 265 (2012).

<sup>5</sup>R. Arsat, M. Breedon, M. Shafiei, P. Spizziri, S. Gilje, R. Kaner, K. Kalantar-zadeh, and W. Wlodarski, *Chem. Phys. Lett.* **467**, 344 (2009).

<sup>6</sup>J. Ebbecke, C. Strobl, and A. Wixforth, *Phys. Rev. B* **70**, 233401 (2004).

<sup>7</sup>M. R. Buitelaar, V. Kashcheyevs, P. J. Leek, V. I. Talyanskii, C. G. Smith, D. Anderson, G. A. C. Jones, J. Wei, and D. H. Cobden, *Phys. Rev. Lett.* **101**, 126803 (2008).

<sup>8</sup>P. Thalmeier, B. Dóra, and K. Ziegler, *Phys. Rev. B* **81**, 041409 (2010).

<sup>9</sup>V. Miseikis, J. E. Cunningham, K. Saeed, R. O'Rourke, and A. G. Davies, *Appl. Phys. Lett.* **100**, 133105 (2012).

<sup>10</sup>C. Berger, Z. Song, X. Li, X. Wu, N. Brown, C. Naud, D. Mayou, T. Li, J. Hass, A. N. Marchenkov, E. H. Conrad, P. N. First, and W. A. de Heer, *Science* **312**, 1191 (2006).

<sup>11</sup>C. Berger, Z. Song, T. Li, X. Li, A. Y. Ogbazghi, R. Feng, Z. Dai, A. N. Marchenkov, E. H. Conrad, P. N. First, and W. A. de Heer, *J. Phys. Chem. B* **108**, 19912 (2004).

<sup>12</sup>M. H. Oliveira, Jr., T. Schumann, M. Ramsteiner, J. M. J. Lopes, and H. Riechert, *Appl. Phys. Lett.* **99**, 111901 (2011).

<sup>13</sup>F. Fromm, M. H. Oliveira, Jr., A. Molina-Sánchez, M. Hundhausen, J. M. J. Lopes, H. Riechert, L. Wirtz, and T. Seyller, *New J. Phys.* **15**, 043031 (2013).

<sup>14</sup>M. M. de Lima, Jr. and P. V. Santos, *Rep. Prog. Phys.* **68**, 1639 (2005).

<sup>15</sup>The calculations use elastic parameters for SiC and ZnO from Refs. 20 and 21, respectively.

<sup>16</sup>H. Suzuura and T. Ando, *Phys. Rev. B* **65**, 235412 (2002).

<sup>17</sup>M. Vozmediano, M. Katsnelson, and F. Guinea, *Phys. Rep.* **496**, 109 (2010).

<sup>18</sup>The values for  $\Delta E_{DP}$  and  $\Phi_{SAW}^{(s)}$  used in the estimation do not take into account piezoelectric screening by charges in EG, which is expected to have similar effects on these two quantities.

<sup>19</sup>K. Kaasbjerg, K. S. Thygesen, and K. W. Jacobsen, *Phys. Rev. B* **85**, 165440 (2012).

<sup>20</sup>K. Kamitani, M. Grimsditch, J. C. Nipko, C.-K. Loong, M. Okada, and I. Kimura, *J. Appl. Phys.* **82**, 3152 (1997).

<sup>21</sup>*Landolt-Börnstein Tables, New Series, Group III: Solid State Physics, Low Frequency Properties of Dielectric Crystals: Elastic Constants*, edited by O. Madelung (Springer-Verlag, Berlin, 1983), Vol. 17a.